A Spatio-Temporal Neural Network for Fine-Scale Wind Field Nowcasting Based on Lidar Observation

Hang Gao ⓘ, Chun Shen ⓘ, Yi Zhou, Xuesong Wang, Pak-Wai Chan, Kai-Kwong Hon ⓘ, Dingfu Zhou, and Jianbing Li ⓘ, *Senior Member, IEEE*

Abstract—**Fine-scale wind field nowcasting is of great significance in air traffic management, power grid operation, and so on. In this article, an indirect wind field nowcasting scheme based on lidar observation is presented, which contains an encoder-forecaster network based on the convolutional long short-term memory with balanced structure and a mask branch. The proposed nowcasting network is trained and evaluated based on the lidar observations throughout 2020 at Hong Kong International Airport. Comprehensive comparison with nine methods including the widely used optical flow technique and classic neural network show the good performance of the new network. It can capture the spatio-temporal features in the lidar observations and obtain better nowcasting results up to 27 min with a resolution of 100 m. The nowcasting errors are smaller than the retrieval errors reported in recent literature, demonstrating that the lidar observation nowcasting based on the new network can get fine-scale wind field nowcasting results with high efficiency.**

Index Terms—**Lidar observation, nowcasting, spatio-temporal, wind field.**

I. INTRODUCTION

WIND field has significant impacts in many aspects, such as wind power generation, aviation safety, and so on. For example, the wind flow drives the turbine and directly determines the power capacity [1], [2], and most of air traffic accidents can be attributed to the severe wind shear or wake vortices encountering during the takeoff and landing phases [3]–[7].

At present, lidar has been widely applied for wind field measurement because of its high accuracy and resolution in dry air condition [8]–[15]. However, a single lidar can only measure the Doppler velocities, say, the velocity components along the line of sight (LOS), which are insufficient to describe the 2-D or 3-D wind field. To estimate the wind vectors in specific areas, such as the aircraft approach and takeoff corridors [16], retrieval methods have been widely studied [17]–[22]. With the existing wind field retrieval methods, the current or previous wind field can be obtained with fine resolution, which can provide instructive information for wind power plant design, aviation safety management, and so on.

To further optimize the air traffic management and power grid operation, accurate wind field prediction is of great significance [23], [24]. In particular, the very short-term nowcasting is desired because hazardous phenomena, such as wind shear and aircraft wake can appear, develop, and dissipate within tens of minutes [23]. Generally, two types of wind field prediction methods have been proposed in recent literatures as follows.

1) *Dynamic Physical Model-Based Methods:* The wind, pressure, density, and temperature in the atmosphere can be described by the laws of fluid mechanics, which include the Navier–Stokes equation, first law of thermodynamics, the ideal gas law, and the mass continuity equation. Numerical methods adopted to solve the equations (or simplified ones) can be referred to as numerical weather prediction (NWP). Data assimilation methods, such as 4-D variation method (4DVAR) [25], [26] and ensemble Kalman filter (EnKF) [27], are broadly used to predict the atmosphere states by combining the NWP with the observations [28]. However, to predict the wind field with fine resolution (∼100 m), the required computation load will be unmanageable for ordinary computers today [29].

2) *Historical Data-Based Methods:* They can be further classified into two categories. The first category includes the methods where only the temporal features are exploited. For example, Markov chain [30], [31], chaotic oscillatory-based neural network (NN) [32], convolutional NN (CNN) [33], Bayesian methodology [34], extreme learning machine [35], Elman NN [24], and so on. However, the wind field varies spatio-temporally, where the spatio-temporal dynamics are important [36] but have yet to be effectively exploited by the approaches in the first category. With the wind speeds measured in neighboring wind farms, the spatio-temporal dependencies are exploited by the methods in the second category, which

Hang Gao, Chun Shen, Xuesong Wang, and Jianbing Li are with the State Key Laboratory of Complex Electromagnetic Environment Effects on Electronics and Information System and the College of Electronic Science and Technology, National University of Defense Technology, Changsha 410073, China (e-mail: gaohang108@163.com; chunshen@nudt.edu.cn; wxs1019@vip.sina.com; jianbingli@nudt.edu.cn).

Yi Zhou is with the Naval Research Academy, Shanghai 200000, China (e-mail: 13818948319@139.com).

Pak-Wai Chan and Kai-Kwong Hon are with the Hong Kong Observatory Hong Kong, China (e-mail: pwchan@hko.gov.hk; kkhon@hko.gov.hk).

Dingfu Zhou is with the South-West Institute of Technical Physics, Chengdu 610000, China (e-mail: df_xh_hou@sina.com).

Digital Object Identifier 10.1109/JSTARS.2022.3189037

includes hybrid methods based on long short-term memory (LSTM) and graph NN [37], [38], Copula theory [39], and CNN [8], [40].

According to the above discussions, the existing historical data-based methods are mainly based on the observations of a single or several monitoring stations, where the observations and predictions are sparsely distributed with low resolution. Benefited from the lidar, it can be reasonably argued that the high-density observations from the lidar can be used for fine-scale wind field nowcasting, which has not been widely studied.

Inspired by the precipitation nowcasting, where the radar echo maps are first predicted, then the future rainfall rate is estimated based on the predictions [41], it is promising to predict the wind field indirectly from the lidar observations: first predict the lidar observations, and then the future wind field is estimated by the broadly studied wind field retrieval methods according to the predictions.

Unfortunately, compared with the wind field retrieval methods, the lidar observation nowcasting has been rarely studied. Therefore, this article will focus on the spatio-temporal nowcasting of the lidar observations. The contributions of this article are as follows.

1) We presented an indirect wind field nowcasting scheme which first predicts the lidar observations, and then the future wind field is estimated by wind field retrieval methods according to the predictions. The feasibility of the scheme is verified by experiments, where the errors in lidar observation nowcasting are found to be smaller than the reported retrieval errors.

2) A novel NN composed of encoder-forecaster network based on convolutional LSTM with balanced structure and a mask branch is proposed for lidar observation nowcasting. To the best of our knowledge, this is the first work that introduces a spatio-temporal deep learning methodology to predict the lidar observations for fine-scale wind field nowcasting.

3) Compared with the traditional optical flow-based method, the newly proposed NN can better capture the spatio-temporal features of the lidar observations. Predictions up to 27 min with a resolution of 100 m can be obtained with higher accuracy.

The rest of this article is organized as follows. In Section II, the NN which is capable to exploit the spatio-temporal features of the lidar observations is described. The field experiment is discussed in Section III. The prediction performances of the NN and that of the traditional methods are compared by comprehensive evaluation and case study in this section.

II. Spatio-Temporal Nowcasting of Lidar Observations

A. Related Work

To forecast the rainfall intensity in a local region, precipitation nowcasting based on the extrapolation of radar echo maps has attracted much attention in meteorological community and machine learning community. There are some similarities between the precipitation nowcasting and lidar observation nowcasting. For example, the two problems involve the complexity of atmosphere, and their fine-scale nowcasting results cannot be obtained by NWP with small calculation cost [42]; the radar echo maps and the lidar observations are with the same dimension; and the spatio-temporal features are important in their dynamics. Therefore, the precipitation nowcasting methods can be helpful for lidar observation nowcasting.

In operational precipitation nowcasting systems, the optical flow-based methods are broadly used for radar echo extrapolation. For example, the variational optical flow technique (VarFlow) [43] has been used to estimate the motion field in the latest precipitation nowcasting system which is operated by Hong Kong Observatory (HKO) [41]. To better utilize the vast amount of historical data, deep learning techniques, such as 3-D CNN [44] and U-Net CNN [45], [46], have been applied. Formulating the precipitation nowcasting problem as an image-to-image translation problem and taking the spatio-temporal features into account, convolutional LSTM (ConvLSTM) [47] and trajectory gated recurrent unit (TrajGRU) [48] have been proposed. ConvLSTM and convolutional GRU (ConvGRU) have shown good performances in extracting spatio-temporal features, and have been widely used in other works [49]–[52]. Apart from the similarities between the precipitation nowcasting and lidar observation nowcasting, we highlight that there are two significant differences between the two problems: 1) the lidar observations present the Doppler velocities with positive and negative values, which may change drastically near the lidar. 2) The lidar or radar sights are inevitably blocked or contaminated at specific areas, such as buildings or mountainous areas, where the observations are unreliable and these areas are referred to as "hole areas." For the multiradar measurement network, the hole areas of a radar may be accurately observed by another one, therefore the hole areas in the radar echo maps are convincingly eliminated by interpolation [53]. For the lidar observations, it is necessary to deal with the hole areas since there is generally only a single lidar for wind field measurement.

According to the above discussions, this article first transforms the lidar observations to gray-level pixels and takes the lidar observation sequences as frame sequences. Then a NN composed of the encoder-forecaster network with balanced structure and a mask branch is established, where the ConvLSTM is adopted in the encoder-forecaster network to exploit the spatio-temporal features. Unlike the past work [48], [54], where the masks are preprepared and are only used to exclude the outliers when computing the loss function, in our work, the mask branch is embedded into the nowcasting network, which is simple and easy to be implanted. We further demonstrate that benefited from the balanced structure and the mask branch, the nowcasting performance of the new model will be efficiently enhanced.

B. Lidar Observation Nowcasting Model

According to the statistics of historical wind velocities, the lidar observations are transformed to gray-level pixels by linear
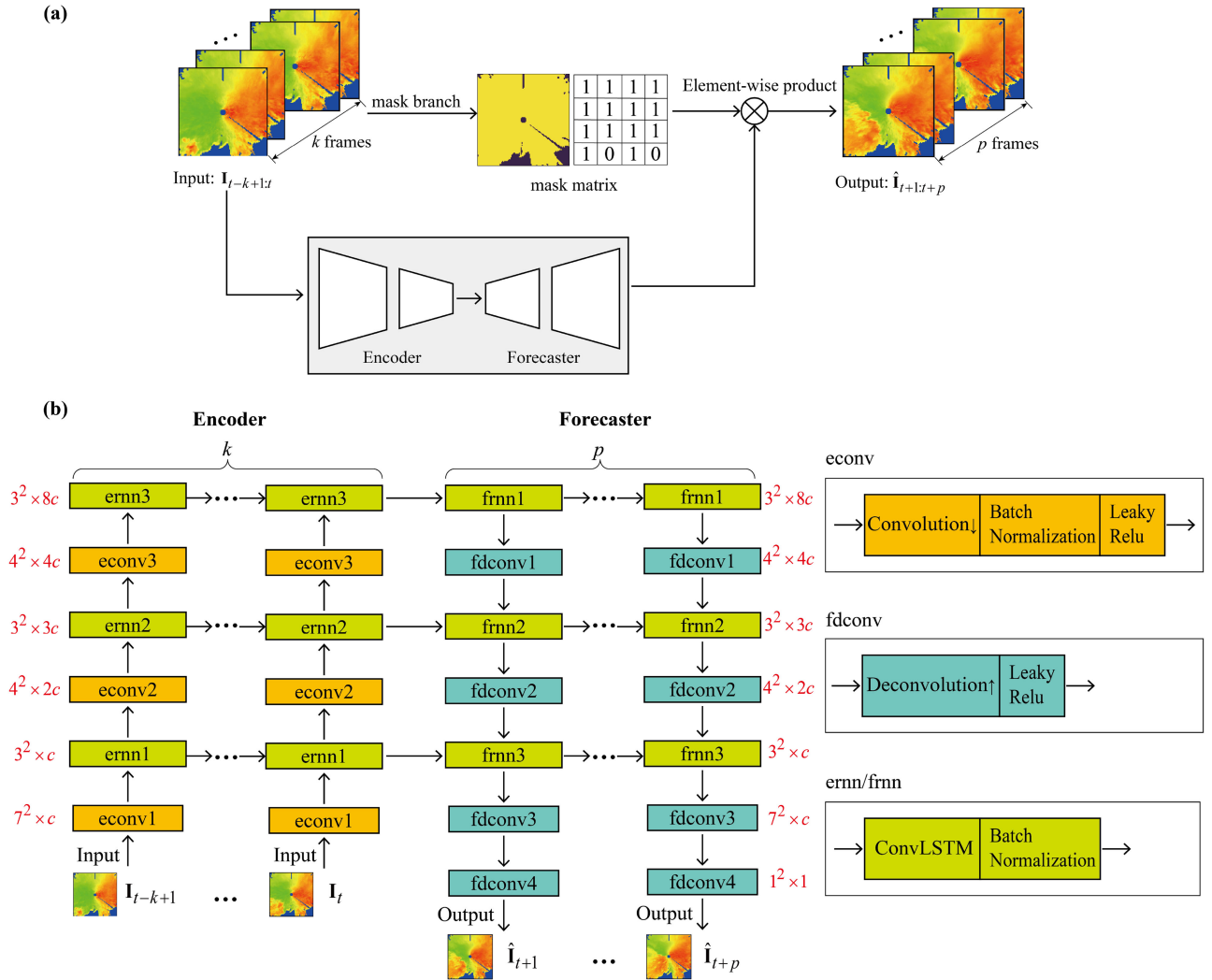
Fig. 1. (a) Framework of the proposed network. (b) Framework of the encoder-forecaster NN with balanced structure. Zeros are fed as input to the ConvLSTMs if the input link is missing. $a^2 \times b$ indicates that the kernel size is $a \times a$, and b is the number of kernels of the convolutional operations. To balance the performance and computing time, the base kernel number c is empirically set as 8.

projection

$$\mathbf{I} = f\left(\mathbf{V}^{\mathrm{D}}\right) = 255 \times \frac{\mathbf{V}^{\mathrm{D}} + 20}{40} \qquad (1)$$

where "20" and "40" stand for the maximum value and the maximum variation range of the lidar observations, respectively, which are obtained by statistical analysis; $\mathbf{V}^{\mathrm{D}}$ is the lidar observation at a single time stamp, which contains all the observations in a full scan. It is noted that the time required for the lidar to conduct a full scan is neglected in this article.

In this way, the lidar observations at different time stamps can be regarded as spatio-temporal frame sequences $\{\mathbf{I}_1, \mathbf{I}_2, \cdots\}$. Therefore, the lidar observation nowcasting can be formulated as a problem of using k observations $\mathbf{I}_{t-k+1:t} \in \mathbb{R}^{k \times H \times W \times 1}$ at a given time stamp t to predict p steps ahead: $\hat{\mathbf{I}}_{t+1:t+p} \in \mathbb{R}^{p \times H \times W \times 1}$, where H and W indicate the height and width of the frame, the last dimension of the frame represents its channel number, which equals to 1 for the gray-level frames.

The network used for lidar observation nowcasting is composed of two parts: 1) an encoder-forecaster NN and 2) a mask branch. The framework is shown in Fig. 1(a).

1) Encoder-Forecaster NN: To exploit the spatio-temporal features in the lidar observations, the ConvLSTM-based encoder-forecaster NN is used, whose structure is similar to that proposed in [47]. The input frame sequence $\mathbf{I}_{t-k+1:t}$ is compressed as low-dimensional spatio-temporal features by the encoder network, which is composed of convolution and ConvLSTM layers. Then the encoded features will be unfolded into the output frame sequence $\hat{\mathbf{I}}_{t+1:t+p}$ by the forecaster network, which is composed of deconvolution and ConvLSTM layers.

According to [55], we have revised the structure of the encoder-forecaster network in [48] to avoid redundant connections. The detailed illustration of the encoder-forecaster NN is shown in Fig. 1(b). Balanced kernel sizes are, respectively, adopted in the encoder and forecaster network, except for the
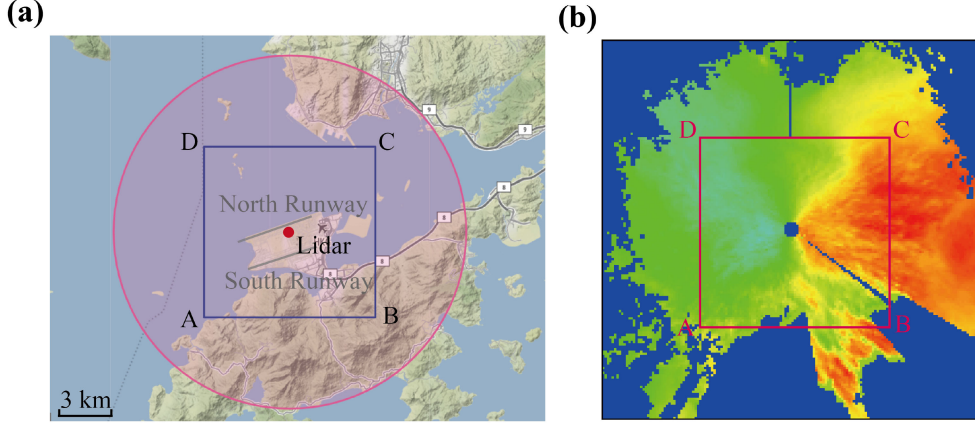
Fig. 2. Illustration of the field campaign. (a) Geometry of the field campaign in HKIA. (b) Example of the lidar observation within $(16\,000\,\text{m})^2$, the cool (warm) colors represent winds toward (away) from the lidar; the dark blue represent the null values.

output layer in the decoder network. In the revised network, the kernel sizes are set as 3×3, 4×4, and 7×7. The variation of the kernel sizes corresponds to multiscale receptive fields in the convolution operator, they can be used to capture the multiscale features in the lidar observations. In the last layer of the forecaster network, an extra "fdconv4" layer is added, where the 1×1 kernel is used to compress the channels of "fdconv3" outputs. The 1×1 kernel has been commonly used in deep learning models, and has been proved to be effective in performance improvement.

2) Mask Branch: Generally, to be distinct from the reliable observations, the pixel values in the hole areas are set as zeros in the frame. If these zero-value pixels are directly used to train the network, lots of effort will be used to make the prediction results in these areas close to 0, which is unnecessary, and the zero-value pixels can mislead other pixels due to the convolution operation. In addition, distinguishing the hole areas from the other areas will be helpful for postprocessing, such as future wind field retrieval.

Therefore, in this article, a mask branch is embedded into the nowcasting network to handle the hole areas. The elements of the mask matrix are either one or zero, which are, respectively, used to identify whether the corresponding observation is reliable. The mask matrix is denoted as $\mathbf{M}_t = (\mathbf{m}_{h,w})_{H \times W}$, whose elements are determined by

$$\mathbf{m}_{h,w} = \prod_{j=t-k+1}^{t} \delta \mathbf{I}_{j,h,w} \tag{2}$$

$$\delta \mathbf{I}_{j,h,w} = \begin{cases} 0, & if\ \mathbf{I}_{j,h,w} = 0 \\ 1, & if\ \mathbf{I}_{j,h,w} \neq 0. \end{cases} \quad h = 1, 2, \ldots H, w = 1, 2, \ldots W \tag{3}$$

By multiplying the output sequence of the encoder-forecaster NN with $\mathbf{M}_t$ by elements, we can obtain the lidar observation nowcasting results with a focus on the reliable areas in the lidar observations.

TABLE I
OUTPUT SIZES OF THE LAYERS IN 2D-CONVLSTM+B+MASK

Encoder	Out size	Forecaster	Out size
input	$\mathbf{10 \times 100 \times 100 \times 1}$	frnn1	$10 \times 16 \times 16 \times 8c$
econv1	$10 \times 96 \times 96 \times c$	fdconv1	$10 \times 32 \times 32 \times 4c$
ernn1	$10 \times 96 \times 96 \times c$	frnn2	$10 \times 32 \times 32 \times 3c$
econv2	$10 \times 32 \times 32 \times 2c$	fdconv2	$10 \times 96 \times 96 \times 2c$
ernn2	$10 \times 32 \times 32 \times 3c$	frnn3	$10 \times 96 \times 96 \times c$
econv3	$10 \times 16 \times 16 \times 4c$	fdconv3	$10 \times 100 \times 100 \times c$
ernn3	$10 \times 16 \times 16 \times 8c$	fdconv4	$\mathbf{10 \times 100 \times 100 \times 1}$

The input and output, both, have 10 frames in the experiment.

III. EXPERIMENT

A. Dataset

To train and evaluate the nowcasting models, a collection of lidar observations throughout 2020 is used. In the field campaign, the lidar was set up near the north runway in the Hong Kong International Airport (HKIA) by HKO. The lidar performs plan position indicator (PPI) scans with an elevation angle of $3°$. It is a long-range lidar whose maximum detection range can reach 10 km, as shown by the red circle in Fig. 2(a). Taking the lidar position as the center, a rectangular grid of 100×100 pixels is established, with each pixel representing an area of $(100\ \text{m})^2$. The rectangular grid covers the north and south runways and corridors, which are the most notable regions in HKIA. The boundary of the grid is shown by the blue rectangle ABCD in Fig. 2(a). The lidar observations are identified by a signal-to-noise ratio (SNR) threshold empirically: if the SNR is lower than the threshold, indicating that the corresponding observation is unreliable and its value will be set to null. An example of the lidar observation is shown in Fig. 2(b). Then the lidar observations are linearly interpolated onto the rectangular grid. It is noted that the interpolation is reliable and accurate since the lidar observations are densely distributed and the null values remain unchanged during the interpolation. Finally, the observations are linearly projected to pixel values by (1), and the null values are set as zeros. Since the transformation is linear for the reliable observations,
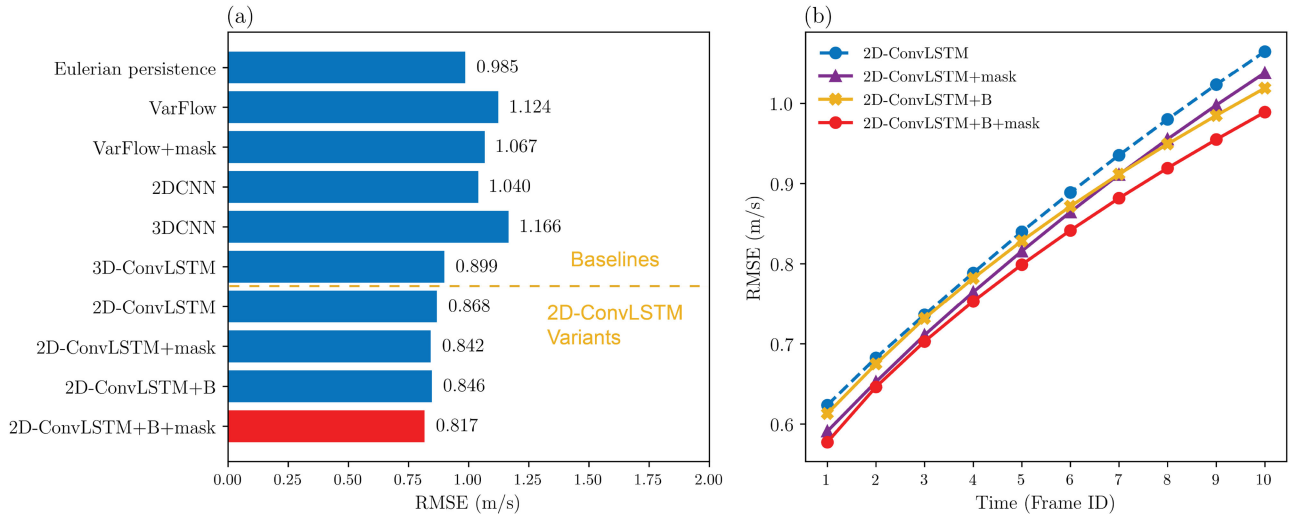
Fig. 3. Comparison of the performance of the ten methods. (a) RMSEs obtained by the methods. (b) RMSEs of the four 2D-ConvLSTM-based variants over time. The abscissa represents the prediction frame ID, varying from 1 to 10, which indicates the time ahead.

it is easy to project the predicted pixel values back to the lidar observations

$$\mathbf{V}^{\mathrm{D}} = f^{-1}(\mathbf{I}) = \frac{\mathbf{I} \times 40}{255} - 20. \tag{4}$$

The time interval between two PPI observations is about 2 min 45 s, therefore, there are about 525 observations in a day. According to [50], for each month, observations in the first day are assigned to the validation set; observations in the last seven days are assigned to the test set; and all other days are assigned to the training set. In the experiment, we aim to predict 10 frames based on 10 input frames, that is to say, $k = p = 10$. As in [47], a 20-frame-wide sliding window is used to generate training, validation, and test sequences from the training, validation, and test sets, respectively. Finally, our lidar observation dataset contains 82 144 training sequences, 4418 validation sequences, and 26 140 test sequences.

B. Comparison Models

To verify the performance of the presented model in lidar observation nowcasting, we have evaluated ten nowcasting methods. They include six baselines and four variants based on 2-D CNN and ConvLSTM layers (abbreviated as 2DCNN-ConvLSTM). The baseline methods include: 1) the Eulerian persistence method, which assumes that the last frame is the prediction for all future states; 2) the traditional VarFlow method, which estimates the motion field from the last two frames; 3) VarFlow method with the mask branch (abbreviated as VarFlow+mask); 4) the original encoder-forecaster network in [48], which is realized by 2-D CNN layers (abbreviated as 2DCNN) or 5) 3-D CNN layers (abbreviated as 3DCNN); and 6) the original encoder-forecaster network in [48] based on the 3-D CNN and ConvLSTM layers (abbreviated as 3D-ConvLSTM), where the convolution and deconvolution are realized by the corresponding 3-D derivations.

For ablation study, the four 2DCNN-ConvLSTM-based variants contain: 1) the original encoder-forecaster network in [48] based on 2DCNN-ConvLSTM (abbreviated as 2D-ConvLSTM); 2) the 2D-ConvLSTM along with the mask branch (abbreviated as 2D-ConvLSTM+mask); 3) the 2DCNN-ConvLSTM with the balanced structure (abbreviated as 2D-ConvLSTM+B); and 4) the 2DCNN-ConvLSTM with the balanced structure and the mask branch (abbreviated as 2D-ConvLSTM+B+mask).

The detailed descriptions of the 2DCNN, 3DCNN, 2D-ConvLSTM, and 3D-ConvLSTM are illustrated in the Appendix Table II–V, respectively. With $k = p = 10$, the output sizes of each layer in the 2D-ConvLSTM+B+mask model are listed in Table I.

C. Training

Since the pixel values and the observations are linearly correlated, the mean square errors (mses) are directly calculated according to the pixel values during the training process. The mse is defined as follows:

$$\mathrm{MSE} = \frac{1}{N_{\mathrm{train}} \times p \times H \times W} \sum_{i=1}^{N_{\mathrm{train}}} \sum_{j=1}^{p} \sum_{h=1}^{H} \sum_{w=1}^{W} \left(\hat{\mathbf{I}}_{i,j} - \mathbf{I}_{i,j} \right)^2 \tag{5}$$

where $N_{\mathrm{train}} = 82\,144$ is the number of training sequences, $\hat{\mathbf{I}}_{i,j}$, $\mathbf{I}_{i,j} \in \mathbb{R}^{H \times W}$ indicate the prediction and the ground truth of the jth frame in the ith training sequence, respectively.

The Adam optimizer with learning rate equal to 10^{-4} is used to optimize the mse during the training process. The mse decreases very quickly, therefore, the number of training epochs is set as 30. All layers except the last one are activated by the leaky ReLU [56] with a negative slope of 0.2.
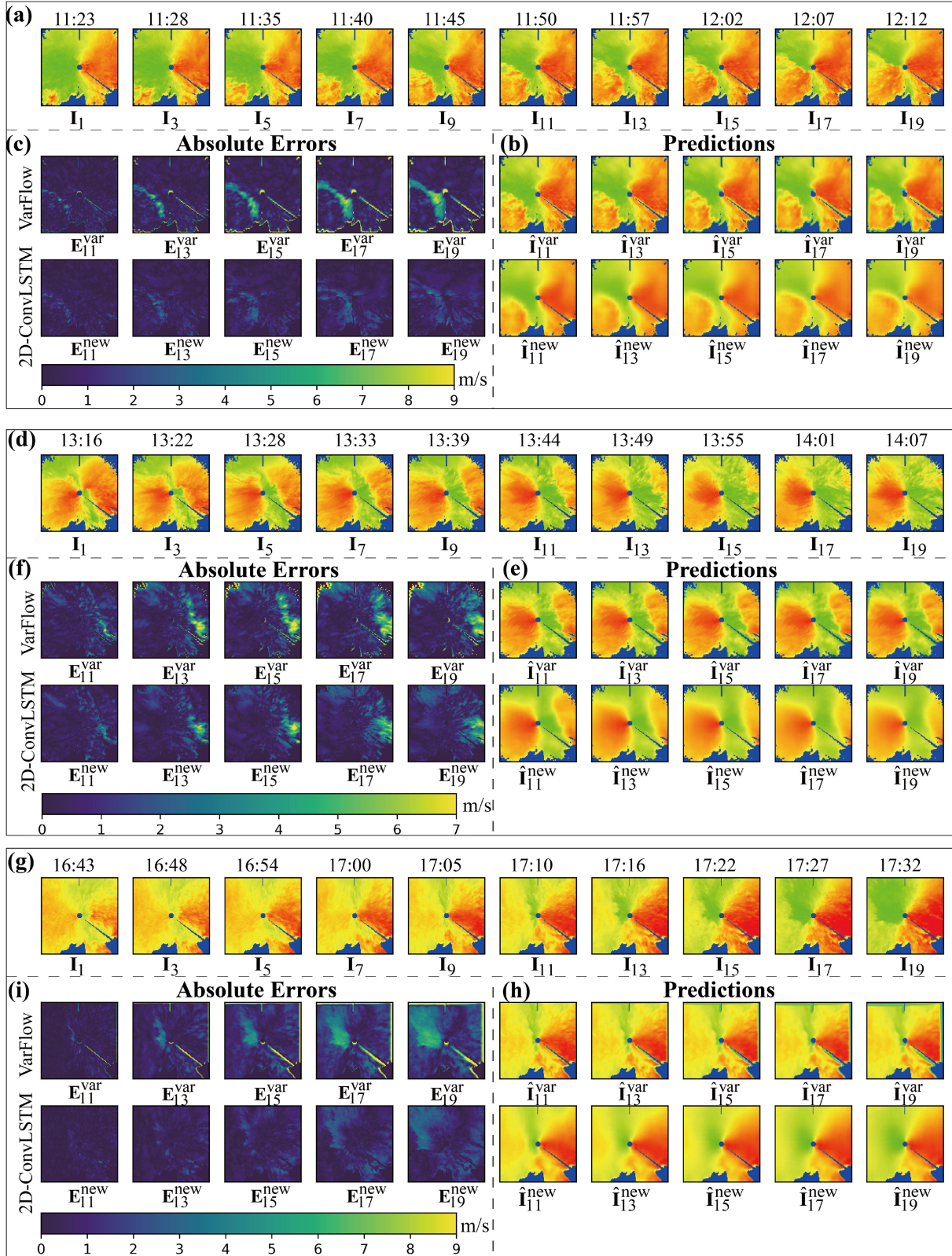
Fig. 4. Comparison between the ground truth and predictions. (a) Ground truth from 11:23 to 12:12 on April 29, 2020, where $\mathbf{I}_1, \ldots, \mathbf{I}_{19}$ represent the ground truth of $1, \ldots, 19$ frames, respectively. (b) Predictions obtained by VarFlow (first row) and 2D-ConvLSTM (second row), where $\hat{\mathbf{I}}_1^{\mathrm{var}}, \ldots, \hat{\mathbf{I}}_{19}^{\mathrm{var}}$ represent the VarFlow predictions; $\hat{\mathbf{I}}_1^{\mathrm{new}}, \ldots, \hat{\mathbf{I}}_{19}^{\mathrm{new}}$ represent the 2D-ConvLSTM predictions. All the ground truth and predictions are subsampled one every two images to improve representation clarity. In the pseudocolor map, the cool (warm) colors represent winds toward (away) from the lidar. (c) Absolute errors between the ground truth and the predictions, where the errors are calculated in terms of the Doppler velocities, $\mathbf{E}_1^{\mathrm{var}}, \ldots, \mathbf{E}_{19}^{\mathrm{var}}$ represent the absolute errors of the VarFlow predictions; $\mathbf{E}_1^{\mathrm{new}}, \ldots, \mathbf{E}_{19}^{\mathrm{new}}$ represent the absolute errors of the 2D-ConvLSTM predictions. (d) Ground truth from 13:16 to 14:07 on April 29, 2020. (g) Ground truth from 16:43 to 17:32 on October 30, 2020. (e), (h) and (f), (i) have the same meaning as that in (b) and (c).
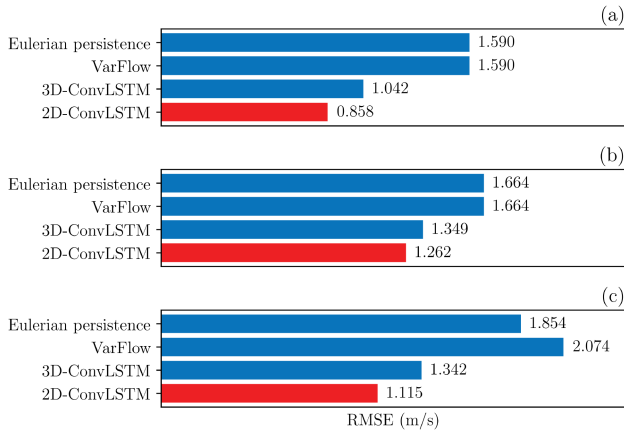
Fig. 5. RMSEs obtained by four methods. For simplification, the VarFlow+mask method and 2D-ConvLSTM+B+mask method are abbreviated as VarFlow and 2D-ConvLSTM method in the comparison. (a)–(c) correspond to Cases 1–3, respectively.

D. Performance Evaluation

According to the test dataset, the nowcasting performance is evaluated by the root mse (RMSE) of the lidar observations

$$\text{RMSE} = \sqrt{\frac{1}{N} \sum_{i=1}^{N_{\text{test}}} \sum_{j=1}^{p} \sum_{h=1}^{H} \sum_{w=1}^{W} \left[\text{mask}\left(f^{-1}(\hat{\mathbf{I}}_{i,j})\right) - \mathbf{V}_{i,j}^{\text{D}} \right]^2}$$

$$(6)$$

where $N = N_{\text{test}} \times p \times H \times W$, with $N_{\text{test}} = 26140$ being the number of test sequences; $\mathbf{V}_{i,j}^{\text{D}} \in \mathbb{R}^{H \times W}$ is the real lidar observation of the jth frame in the ith test sequence, $\text{mask}(\cdot)$ indicates to only take the predictions in the reliable areas into account. $f^{-1}(\cdot)$ indicates to project the predicted pixel values back to the lidar observations, which is defined in (4).

The RMSEs obtained by the ten methods are illustrated in Fig. 3(a), from which, the following are observed.

1) The RMSE obtained by Eulerian persistence is smaller than that obtained by the other six baseline methods except for the 3D-ConvLSTM, because most of wind fields in the dataset are uniform and stable during the leading time.

2) Except for the 3DCNN method, the NN models can predict the lidar observations with a higher accuracy than the traditional VarFlow method. The poor performance of the VarFlow method may be caused by the errors introduced by the motion field estimation.

3) Without the mask branch and the balanced structure, the 2D-ConvLSTM and 3D-ConvLSTM can obtain the most accurate predictions among the first seven nowcasting methods in Fig. 3(a). It indicates that the ConvLSTM framework can help to exploit the spatio-temporal features in the sequences, which can efficiently improve the nowcasting performance.

4) Based on the 2D-ConvLSTM, we have studied the performance enhancement provided by the balanced structure and the mask branch, respectively. It is found that the RMSE obtained by the last model is the smallest one compared to that of the other models in Fig. 3(a). Therefore, the

2D-ConvLSTM with the balanced structure and the mask branch (2D-ConvLSTM+B+mask) is more favorable in lidar observation nowcasting.

The RMSEs of the four 2D-ConvLSTM variants over time are further compared in Fig. 3(b). We find that the RMSEs obtained by the 2D-ConvLSTM+B+mask model over time are the smallest ones compared with that obtained by other variant methods; that is to say, the 2D-ConvLSTM+B+mask model outperforms other models. The relevance between the future wind field with the lidar observations decreases over time, resulting in the performance decline of the four nowcasting methods, which is common and reasonable in nowcasting and prediction problems. Specifically, it is noted that, compared with the models with the original structure, the new balanced structure can slow down the accumulation of the errors over time; for example, the yellow line has a smaller slope than the blue dashed line in Fig. 3(b); compared with the models without the mask branch, a general reduction of the RMSEs is a benefit of the mask branch; for example, the purple line has an overall reduction compared with the blue dashed line in Fig. 3(b).

In our earlier work, the same lidar observations and synchronous *in situ* observations were assimilated to retrieve the wind field [57]. The reported retrieval RMSE is about 1.5 m/s, which is obviously bigger than the nowcasting RMSE in Fig. 3(b). Therefore, it can be reasonably deduced that, the future wind field can be predicted indirectly through lidar observation nowcasting, and the prediction error will largely depend on the retrieval methods.

E. Case Study

It is noted that the RMSEs are comprehensively evaluated on the whole test dataset, where most wind fields are stable and calm. In particular, for the most concerned wind fields in aviation safety, the performances of the VarFlow+mask method and 2D-ConvLSTM+B+mask model under three typical wind shear conditions are further compared. Wind shear is recognized as one of the most common aviation hazards. It can lead to drastic changes in the wind field within tens of minutes. Case 1 and 2 show a complete evolution process of wind shear from formation to dissipation, Case 3 shows the dissipation process of wind shear along with significant wind speed enhancement. For simplification, the VarFlow+mask method and 2D-ConvLSTM+B+mask method are further abbreviated as VarFlow and 2D-ConvLSTM method in case study.

1) Case 1: The ground truth from 11:23 to 12:12 on April 29, 2020 is shown in Fig. 4(a). From $\mathbf{I}_1$, we find that the wind field is almost uniform at the beginning, and it flows from the left to the right of the frame. Later, the wind shear is initiated, which is shown by the inverse Doppler velocities in the left side of the frames. The center of the wind shear moves to the lidar position in $\mathbf{I}_{19}$. The prediction results obtained by VarFlow and 2D-ConvLSTM are shown in the first and second rows in Fig. 4(b), respectively. We can find that, compared with the ground truth, the predictions obtained by VarFlow are all similar to the last input frame, which indicates that the predictions failed to capture the spatio-temporal features of the wind shear due

to the underestimated motion field. However, the predictions obtained by 2D-ConvLSTM can represent the evolution of wind shear to some extent, because a certain amount of complex spatio-temporal patterns are contained in the training dataset during the training process of 2D-ConvLSTM. It should be noted that, the predictions of the 2D-ConvLSTM model are blurred, which may be caused by the mse loss in model training [58] and the inherent uncertainties of the lidar observations due to the randomness in the wind field evolution [47]. The blurry phenomenon can be handled by modifying the loss function and the network framework, which will be studied in the future work.

The absolute errors between the ground truth and the predictions are compared in Fig. 4(c). We can find that the prediction errors of the two methods increase over time, which coincides with Fig. 3(b). The errors of each frame mainly come from the front part of the warm area, where the observations are drastically changed. In the traditional VarFlow method, the errors also occur at the edges of the hole areas. The reason is that the pixel values in the hole areas are zeros, which are distinct from the others and may introduce errors in the motion field estimation.

The RMSEs obtained by the methods are compared in Fig. 5(a), where four methods are used for comparison according to their good performance in Fig. 3(a), these methods include Eulerian persistence, VarFlow (VarFlow+mask), 3D-ConvLSTM, and 2D-ConvLSTM (2D-ConvLSTM+B+mask). From the comparison, it can be found that all the RMSEs obtained by the four methods are slightly bigger than that in Fig. 3(a). This is reasonable because wind shear events, which can be recognized as extreme events, are rarer than stable wind fields, resulting in a small proportion of extreme events in the training dataset. This statement can be verified by Fig. 4(c), from which we can find that the nowcasting errors mainly come from the areas where the observations change drastically. Moreover, the 2D-ConvLSTM consistently outperforms the baseline methods. It is noted that the first two baseline methods have the same RMSE, because in the VarFlow method the nearest interpolation always ignores the changes brought by the underestimated motion field.

2) Case 2: After the wind shear in Case 1 is fully evolved, it gradually dissipates, which is depicted in case 2. Comparing I_{19} in Fig. 4(d) with Fig. 4(a) I_1, it is obvious that, caused by the evolution of wind shear, the direction of the uniform wind field was completely reversed within 11:23 to 14:07. The reversion can seriously impact the aircraft takeoff and landing phases, and its accurate prediction is of great significance in aviation safety. As the conclusion in Case 1 shows, the 2D-ConvLSTM can better capture the spatio-temporal dynamic features of wind shear than the VarFlow method. Moreover, the absolute errors mainly occur at the areas where the observations change dramatically.

The RMSEs obtained by the four methods are compared in Fig. 5(b), which is similar to that shown in Fig. 5(a) for Case 1.

3) Case 3: Similar to Case 2, a dissipation process of wind shear is recorded in Case 3. The difference is that besides the dissipation, the wind speed is significantly enhanced, as shown by the darker red in the last frames. Case 3 aims to evaluate the nowcasting performance when there are significant changes in wind speed and direction. From Fig. 4(g), we can find that

the wind speed enhancement can be correctly predicted by both the VarFlow method and 2D-ConvLSTM method. However, the variation in wind direction, that is the dissipation of wind shear, can only be predicted by the 2D-ConvLSTM method. Therefore, the 2D-ConvLSTM method can successfully predict the dynamical evolutions of wind direction and speed with small errors.

According to the RMSEs shown in Fig. 5(c), it is noted that the VarFlow method has the biggest RMSE among the methods. The reason is that although the mask branch is introduced in the VarFlow method, the estimated motion field can affect the entire frame including the hole areas. It indicates that the hole areas in the lidar observations cannot be well handled by the VarFlow method. This statement can be verified from Fig. 4(i), where it is found that the big absolute errors of the VarFlow method occur at the edge of the hole areas. Furthermore, as expected, the 2D-ConvLSTM can best predict the lidar observations when the wind field changes dynamically.

IV. CONCLUSION

To forecast the near future wind field with high resolution, this article proposes to indirectly predict the wind field based on lidar observation nowcasting. Regarding the speciality in lidar observation nowcasting, a new NN is proposed, which contains the ConvLSTM-based encoder-forecaster network with balanced structure and a mask branch. Once trained, the network can quickly predict the future lidar observations for the next ten time stamps, that is up to 27 min in advance. To the best of our knowledge, this is the first work that uses the spatio-temporal NN for lidar observation nowcasting and successfully validates the feasibility of fine-scale wind field nowcasting based on lidar observations. The predicted lidar observations can be directly used for wind hazard warning, and can be further used to retrieve the future wind field for other prediction products.

From the experiment results, we find that the 2D-ConvLSTM with the balanced structure and the mask branch outperforms the baseline methods and other 2DCNN-ConvLSTM-based variant methods. It can well capture the spatio-temporal features and provide more accurate predictions of the lidar observations. The designed balanced structure and the mask branch can both improve the nowcasting performance.

In our work, the network is trained on the historical observations provided by the long range lidar in HKIA. To extend the framework to other measurement conditions, transfer learning can be used to quickly adjust the trained nowcasting network to make it suitable for actual conditions. Further studies include alleviating the blurry phenomenon in the predictions, and optimizing the framework for better nowcasting performance especially under extreme conditions.

APPENDIX
DETAILED STRUCTURE OF THE NEURAL NETWORKS

The details of the 2DCNN, 3DCNN, 2D-ConvLSTM, and 3D-ConvLSTM models are listed in Tables II–V, respectively.

TABLE II
DETAILS OF 2DCNN MODEL WITH $c = 128$

Name	Kernel	Channel	Stride	Regularizer	In/Out size
econv1	7×7	c	(1,1)	BN	$100 \times 100 \times 10/96 \times 96 \times c$
econv2	4×4	c	(3,3)	BN	$96 \times 96 \times c/32 \times 32 \times c$
econv3	4×4	$2c$	(2,2)	BN	$32 \times 32 \times c/16 \times 16 \times 2c$
econv4	4×4	$3c$	(2,2)	BN	$16 \times 16 \times 2c/8 \times 8 \times 3c$
econv5	4×4	$4c$	(2,2)	BN	$8 \times 8 \times 3c/4 \times 4 \times 4c$
fdconv1	1×1	$8c$	(1,1)	-	$4 \times 4 \times 4c/4 \times 4 \times 8c$
fdconv2	4×4	$4c$	(2,2)	-	$4 \times 4 \times 8c/8 \times 8 \times 4c$
fdconv3	4×4	$3c$	(2,2)	-	$8 \times 8 \times 4c/16 \times 16 \times 3c$
fdconv4	4×4	$2c$	(2,2)	-	$16 \times 16 \times 3c/32 \times 32 \times 2c$
fdconv5	4×4	c	(3,3)	-	$32 \times 32 \times 2c/96 \times 96 \times c$
fdconv6	5×5	10	(1,1)	-	$96 \times 96 \times c/100 \times 100 \times 10$

"BN" stands for batch normalization, and "econv" and "fdconv" are as illustrated in Fig. 1(a).

TABLE III
DETAILS OF 3DCNN MODEL WITH $c = 64$

Name	Kernel	Channel	Stride	Regularizer	In/Out size
econv1	$7 \times 7 \times 7$	c	(1,1,1)	BN	$100 \times 100 \times 10 \times 1/96 \times 96 \times 4 \times c$
econv2	$4 \times 4 \times 1$	c	(3,3,1)	BN	$96 \times 96 \times 4 \times c/32 \times 32 \times 6 \times c$
econv3	$4 \times 4 \times 4$	$2c$	(2,2,2)	BN	$32 \times 32 \times 6 \times c/16 \times 16 \times 2 \times 2c$
econv4	$4 \times 4 \times 4$	$3c$	(2,2,2)	BN	$16 \times 16 \times 2 \times 2c/8 \times 8 \times 1 \times 3c$
econv5	$4 \times 4 \times 4$	$4c$	(2,2,2)	BN	$8 \times 8 \times 1 \times 3c/4 \times 4 \times 1 \times 4c$
fdconv1	$1 \times 1 \times 2$	$8c$	(1,1,1)	-	$4 \times 4 \times 1 \times 4c/4 \times 4 \times 2 \times 8c$
fdconv2	$4 \times 4 \times 4$	$4c$	(2,2,2)	-	$4 \times 4 \times 2 \times 8c/8 \times 8 \times 4 \times 4c$
fdconv3	$4 \times 4 \times 4$	$3c$	(2,2,1)	-	$8 \times 8 \times 4 \times 4c/16 \times 16 \times 8 \times 3c$
fdconv4	$4 \times 4 \times 4$	$2c$	(2,2,1)	-	$16 \times 16 \times 8 \times 3c/32 \times 32 \times 8 \times 2c$
fdconv5	$4 \times 4 \times 3$	c	(3,3,1)	-	$32 \times 32 \times 8 \times 2c/96 \times 96 \times 10 \times c$
fdconv6	$5 \times 5 \times 1$	1	(1,1,1)	-	$96 \times 96 \times 10 \times c/100 \times 100 \times 10 \times 1$

TABLE IV
DETAILS OF 2D-CONVLSTM MODEL WITH $c = 8$

Name	Kernel	Channel	Stride	Regularizer	In/Out size
econv1	7×7	c	(1,1)	BN	$10 \times 100 \times 100 \times 1/10 \times 96 \times 96 \times c$
ernn1	3×3	c	(1,1)	BN	$10 \times 96 \times 96 \times c/10 \times 96 \times 96 \times c$
econv2	4×4	$2c$	(3,3)	BN	$10 \times 96 \times 96 \times c/10 \times 32 \times 32 \times 2c$
ernn2	3×3	$3c$	(1,1)	BN	$10 \times 32 \times 32 \times 2c/10 \times 32 \times 32 \times 3c$
econv3	4×4	$4c$	(2,2)	BN	$10 \times 32 \times 32 \times 3c/10 \times 16 \times 16 \times 4c$
ernn3	3×3	$8c$	(1,1)	BN	$10 \times 16 \times 16 \times 4c/10 \times 16 \times 16 \times 8c$
frnn1	3×3	$8c$	(1,1)	BN	$10 \times 16 \times 16 \times 8c/10 \times 16 \times 16 \times 8c$
fdconv1	4×4	$4c$	(2,2)	-	$10 \times 16 \times 16 \times 8c/10 \times 32 \times 32 \times 4c$
frnn2	3×3	$3c$	(1,1)	BN	$10 \times 32 \times 32 \times 4c/10 \times 32 \times 32 \times 3c$
fdconv2	4×4	$2c$	(3,3)	-	$10 \times 32 \times 32 \times 3c/10 \times 96 \times 96 \times 2c$
frnn3	3×3	c	(1,1)	BN	$10 \times 96 \times 96 \times 2c/10 \times 96 \times 96 \times c$
fdconv3	3×3	c	(1,1)	-	$10 \times 96 \times 96 \times c/10 \times 100 \times 100 \times c$
fdconv4	3×3	1	(1,1)	-	$10 \times 100 \times 100 \times c/10 \times 100 \times 100 \times 1$

"ernn" and "frnn" are as Illustrated in Fig. 1(a).

TABLE V
DETAILS OF 3D-CONVLSTM MODEL WITH $c = 8$

Name	Kernel	Channel	Stride	Regularizer	In/Out size
econv1	$3 \times 7 \times 7$	c	(1,1,1)	BN	$10 \times 100 \times 100 \times 1/8 \times 96 \times 96 \times c$
ernn1	3×3	c	(1,1)	BN	$8 \times 96 \times 96 \times c/8 \times 96 \times 96 \times c$
econv2	$4 \times 4 \times 4$	$2c$	(2,3,3)	BN	$8 \times 96 \times 96 \times c/4 \times 32 \times 32 \times 2c$
ernn2	3×3	$3c$	(1,1)	BN	$4 \times 32 \times 32 \times 2c/4 \times 32 \times 32 \times 3c$
econv3	$4 \times 4 \times 4$	$4c$	(2,2,2)	BN	$4 \times 32 \times 32 \times 3c/1 \times 16 \times 16 \times 4c$
ernn3	3×3	$8c$	(1,1)	BN	$1 \times 16 \times 16 \times 4c/1 \times 16 \times 16 \times 8c$
frnn1	3×3	$8c$	(1,1)	BN	$1 \times 16 \times 16 \times 8c/1 \times 16 \times 16 \times 8c$
fdconv1	$4 \times 4 \times 4$	$4c$	(4,2,2)	-	$1 \times 16 \times 16 \times 8c/4 \times 32 \times 32 \times 4c$
frnn2	3×3	$3c$	(1,1)	BN	$4 \times 32 \times 32 \times 4c/4 \times 32 \times 32 \times 3c$
fdconv2	$4 \times 4 \times 4$	$2c$	(2,3,3)	-	$4 \times 32 \times 32 \times 3c/8 \times 96 \times 96 \times 2c$
frnn3	3×3	c	(1,1)	BN	$8 \times 96 \times 96 \times 2c/8 \times 96 \times 96 \times c$
fdconv3	$1 \times 3 \times 3$	c	(1,1,1)	-	$8 \times 96 \times 96 \times c/10 \times 100 \times 100 \times c$
fdconv4	$3 \times 3 \times 3$	1	(1,1,1)	-	$10 \times 100 \times 100 \times c/10 \times 100 \times 100 \times 1$

REFERENCES

[1] P. Veers *et al.*, "Grand challenges in the science of wind energy," *Science*, vol. 366, no. 6464, 2019, Art. no. eaau2027.

[2] H. S. Dhiman, D. Deb, and V. E. Balas, "Chapter 3—Paradigms in wind forecasting," in *Supervised Machine Learning in Wind Forecasting and Ramp Event Prediction (Wind Energy Engineering)*, H. S. Dhiman, D. Deb, and V. E. Balas, Eds. New York, NY, USA: Academic, 2020, ch. 3, pp. 23–39.

[3] C. Keohan, "Ground-based wind shear detection systems have become vital to safe operations," *Icao J.*, vol. 62, no. 2, pp. 16–19, 2007.

[4] P. R. Veillette, "Data show that US wake-turbulence accidents are most frequent at low altitude and during approach and landing," *Flight Saf. Dig.*, vol. 21, no. 3/4, pp. 1–47, 2002.

[5] T. Gerz *et al.*, "Research towards a wake-vortex advisory system for optimal aircraft spacing," *Comptes Rendus Physique*, vol. 6, no. 4/5, pp. 501–523, 2005.

[6] R. G. Hallowell and J. Y. N. Cho, "Wind shear system cost benefit analysis," *Lincoln Lab. J.*, vol. 18, no. 2, pp. 47–68, 2010.

[7] F. Barbaresco *et al.*, "Monitoring wind, turbulence and aircraft wake vortices by high resolution RADAR and LIDAR remote sensors in all weather conditions," in *Proc. URSI Sci. Days*, 2015, pp. 81–110.

[8] S. Woo, J. Park, J. Park, and L. Manuel, "Wind field-based short-term turbine response forecasting by stacked dilated convolutional LSTMs," *IEEE Trans. Sustain. Energy*, vol. 11, no. 4, pp. 2294–2304, Oct. 2020.

[9] R. Frehlich, Y. Meillier, and M. L. Jensen, "Measurements of boundary layer profiles with in situ sensors and Doppler lidar," *J. Atmospheric Ocean. Technol.*, vol. 25, no. 8, pp. 1328–1340, 2008.

[10] V. A. Banakh and I. N. Smalikho, "Lidar estimates of the anisotropy of wind turbulence in a stable atmospheric boundary layer," *Remote Sens.*, vol. 11, no. 18, 2019, Art. no. 2115.

[11] E. Päschke, R. Leinweber, and V. Lehmann, "An assessment of the performance of a 1.5 μm Doppler lidar for operational vertical wind profiling based on a 1-year trial," *Atmospheric Meas. Techn.*, vol. 8, no. 6, pp. 2251–2266, 2015.

[12] J. Li, C. Shen, H. Gao, P. Chan, K. Hon, and X. Wang, "Path integration (PI) method for the parameter-retrieval of aircraft wake vortex by lidar," *Opt. Exp.*, vol. 28, no. 3, pp. 4286–4306, 2020.

[13] H. Gao, J. Li, P. Chan, K. Hon, and X. Wang, "Parameter-retrieval of dry-air wake vortices with a scanning Doppler lidar," *Opt. Exp.*, vol. 26, no. 13, pp. 16377–16392, 2018.

[14] L. Thobois, J. P. Cariou, and I. Gultepe, "Review of lidar-based applications for aviation weather," *Pure Appl. Geophys.*, vol. 176, no. 5, pp. 1959–1976, 2019.

[15] R. Frehlich and N. Kelley, "Measurements of wind and turbulence profiles with scanning Doppler lidar for wind energy applications," *IEEE J. Sel. Topics Appl. Earth Observ. Remote Sens.*, vol. 1, no. 1, pp. 42–47, Mar. 2008.

[16] O. Nijhuis *et al.*, "Wind hazard and turbulence monitoring at airports with lidar, radar, and mode-s downlinks the UFO project," *Bull. Amer. Meteorological Soc.*, vol. 99, no. 11, pp. 2275–2294, 2018.

[17] P. Waldteufel and H. Corbin, "On the analysis of single-Doppler radar data," *J. Appl. Meteorol.*, vol. 18, no. 4, pp. 532–542, 1979.

[18] C. J. Qiu, A. M. Shao, S. Liu, and Q. Xu, "A two-step variational method for three-dimensional wind retrieval from single Doppler radar," *Meteorol. Atmospheric Phys.*, vol. 91, no. 1/4, pp. 1–8, Jan. 2006.

[19] J. Gao, M. Xue, S. Y. Lee, A. Shapiro, Q. Xu, and K. K. Droegemeier, "A three-dimensional variational single-Doppler velocity retrieval method with simple conservation equation constraint," *Meteorol. Atmospheric Phys.*, vol. 94, no. 1, pp. 11–26, 2006.

[20] N. Li, M. Wei, Y. Yu, and W. Zhang, "Evaluation of a support vector machine-based single-Doppler wind retrieval algorithm," *J. Atmospheric Ocean. Technol.*, vol. 34, no. 8, pp. 1749–1761, Aug. 2017.

[21] N. Li, M. Wei, X. Mu, and C. Zhao, "A support vector machine-based VVP wind retrieval method," *Atmospheric Sci. Lett.*, vol. 16, no. 3, pp. 331–337, 2015.

[22] D. J. Boccippio, "A diagnostic analysis of the VVP single-Doppler retrieval technique," *J. Atmospheric Ocean. Technol.*, vol. 12, no. 2, pp. 230–248, 1995.

[23] J. Mccarthy, J. W. Wilson, and M. R. Hjelmfelt, "Operational wind shear detection and warning: The 'CLAWS' experience at Denver and future objectives," in *Proc. 23rd Conf. Radar Meteorol.*, 1986, pp. 65–69.

[24] J. Wang, S. Wang, and W. Yang, "A novel non-linear combination system for short-term wind speed forecast," *Renewable Energy*, vol. 143, pp. 1172–1192, 2019.

[25] F. A. Rihan, C. G. Collier, and I. Roulstone, "Four-dimensional variational data assimilation for Doppler radar wind data," *J. Comput. Appl. Math.*, vol. 176, no. 1, pp. 15–34, Apr. 2005.

[26] A. C. Oude Nijhuis, O. K. Krasnov, C. M. Unal, H. W. Russchenberg, and A. Yarovoy, "Outlook for a new wind field retrieval technique: The 4D-Var wind retrieval," in *Proc. Int. Radar Conf.*, 2014, pp. 1–6.

[27] G. Evensen, "The ensemble Kalman filter: Theoretical formulation and practical implementation," *Ocean Dyn.*, vol. 53, no. 4, pp. 343–367, 2003.

[28] O. Bousquet, T. Montmerle, and P. Tabary, "Using operationally synthesized multiple-doppler winds for high resolution horizontal wind forecast verification," *Geophys. Res. Lett.*, vol. 35, no. 10, pp. 1–6, 2008.

[29] P. Bauer, A. Thorpe, and G. Brunet, "The quiet revolution of numerical weather prediction," *Nature*, vol. 525, no. 7567, pp. 47–55, 2015.

[30] H. Kantz, D. Holstein, M. Ragwitz, and N. K. Vitanov, "Markov chain model for turbulent wind speed data," *Physica A: Stat. Mech. Appl.*, vol. 342, no. 1/2, pp. 315–321, 2004.

[31] A. D. Sahin and Z. Sen, "First-order Markov chain approach to wind speed modelling," *J. Wind Eng. Ind. Aerodynnamics*, vol. 89, no. 3/4, pp. 263–269, 2001.

[32] K. M. Kwong, F. W. Tee, J. N. Liu, and P. W. Chan, "Implementation and applications of chaotic oscillatory based neural network for wind prediction problems," *Atmosfera*, vol. 24, no. 4, pp. 397–416, 2011.

[33] Y. Y. Hong and C. L. P. P. Rioflorido, "A hybrid deep learning-based neural network for 24-h ahead wind power forecasting," *Appl. Energy*, vol. 250, pp. 530–539, 2019.

[34] M. S. Miranda and R. W. Dunn, "One-hour-ahead wind speed prediction using a Bayesian methodology," in *Proc. Power Eng. Soc. Gen. Meeting*, 2006, pp. 1–6.

[35] C. Wu, J. Wang, X. Chen, P. Du, and W. Yang, "A novel hybrid system based on multi-objective optimization for wind speed forecasting," *Renewable Energy*, vol. 146, pp. 149–165, 2020.

[36] M. Reichstein, "Deep learning and process understanding for data-driven Earth system science," *Nature*, vol. 566, no. 7743, pp. 195–204, 2019.

[37] M. Khodayar and J. Wang, "Spatio-temporal graph deep neural network for short-term wind speed forecasting," *IEEE Trans. Sustain. Energy*, vol. 10, no. 2, pp. 670–681, Apr. 2019.

[38] J. Bi, H. Li, H. Yuan, and S. Duanmu, "A spatio-temporal prediction method of wind energy in green cloud data centers," in *Proc. IEEE Int. Conf. Syst., Man, Cybern.*, 2022, pp. 570–575.

[39] B. Zhang, Q. Li, H. Pang, J. Xu, and Y. Huang, "Wind speed prediction for wind farm based on Clayton Copula function and deep learning fusion," in *Proc. IEEE 4th Int. Elect. Energy Conf.*, 2021, pp. 1–6.

[40] Q. Zhu *et al.*, "Learning temporal and spatial correlations jointly: A unified framework for wind speed prediction," *IEEE Trans. Sustain. Energy*, vol. 11, no. 1, pp. 509–523, Jan. 2020.

[41] W. C. Woo and W. K. Wong, "Operational application of optical flow techniques to radar-based rainfall nowcasting," *Atmosphere*, vol. 8, no. 3, 2017, Art. no. 48.

[42] J. Sun *et al.*, "Use of NWP for nowcasting convective precipitation: Recent progress and challenges," *Bull. Amer. Meteorological Soc.*, vol. 95, no. 3, pp. 409–426, 2014.

[43] A. Bruhn, J. Weickert, C. Feddern, T. Kohlberger, and C. Schnörr, "Variational optical flow computation in real time," *IEEE Trans. Image Process.*, vol. 14, no. 5, pp. 608–615, May 2005.

[44] W. Zhang, L. Han, J. Sun, H. Guo, and J. Dai, "Application of multichannel 3D-cube successive convolution network for convective storm nowcasting," in *Proc. IEEE Int. Conf. Big Data*, 2019, pp. 1705–1710.

[45] S. Agrawal, L. Barrington, C. Bromberg, J. Burge, C. Gazen, and J. Hickey, "Machine learning for precipitation nowcasting from radar images," in Proc. 33rd Conf. Neural Inf. Process. Syst., 2019, pp. 1–6.

[46] X. Pan, Y. Lu, K. Zhao, H. Huang, M. Wang, and H. Chen, "Improving nowcasting of convective development by incorporating polarimetric radar variables into a deep-learning model," *Geophysical Res. Lett.*, vol. 48, no. 21, 2021, Art. no. e2021GL095302.

[47] X. Shi, Z. Chen, H. Wang, D.-Y. Yeung, W.-k. Wong, and W.-c. Woo, "Convolutional LSTM network: A machine learning approach for precipitation nowcasting," in *Proc. 28th Int. Conf. Neural Inf. Process. Syst.*, 2015, pp. 802–810.

[48] X. Shi *et al.*, "Deep learning for precipitation nowcasting: A benchmark and a new model," in *Proc. Adv. Neural Inf. Process. Syst.*, 2017, pp. 5618–5628.

[49] C. K. Sønderby *et al.*, "MetNet: A neural weather model for precipitation forecasting," 2020, *arXiv:2003.12140*.

[50] S. Ravuri *et al.*, "Skilful precipitation nowcasting using deep generative models of radar," *Nature*, vol. 597, no. 7878, pp. 672–677, 2021.

[51] Y. Cao *et al.*, "Precipitation nowcasting with star-bridge networks," 2019, *arXiv:1907.08069*.

[52] T. Xiong, J. He, H. Wang, X. Tang, Z. Shi, and Q. Zeng, "Contextual SA-attention convolutional LSTM for precipitation nowcasting: A spatiotemporal sequence forecasting view," *IEEE J. Sel. Topics Appl. Earth Observ. Remote Sens.*, vol. 14, pp. 12479–12491, 2021, doi: 10.1109/JSTARS.2021.3128522.

[53] J. Zhang, K. Howard, W. Xia, C. Langston, S. Wang, and Y. Qin, "Three-dimensional high-resolution national radar mosaic," in *Proc. Conf. Aviation, Range, Aerosp. Meteorol.*, 2004, pp. 123–127.

[54] G. Franch, D. Nerini, M. Pendesini, L. Coviello, G. Jurman, and C. Furlanello, "Precipitation nowcasting with orographic enhanced stacked generalization: Improving deep learning predictions on extreme events," *Atmosphere*, vol. 11, no. 3, 2020, Art. no. 267.

[55] Q. K. Tran and S. K. Song, "Computer vision in precipitation nowcasting: Applying image quality assessment metrics for training deep neural networks," *Atmosphere*, vol. 10, no. 5, 2019, Art. no. 244.

[56] A. L. Maas, A. Y. Hannun, and A. Y. Ng, "Rectifier nonlinearities improve neural network acoustic models," in Proc. ICML Workshop Deep Learn. Audio, Speech Lang. Process., vol. 28, 2013, pp. 1–6.

[57] H. Gao, J. Zhou, P.-W. Chan, K.-K. Hon, and J. Li, "A hybrid method for fine-scale wind field retrieval based on machine learning and data assimilation," IEEE Trans. Geosci. Remote Sens., vol. 60, 2022, Art. no. 4107012, doi: 10.1109/TGRS.2022.3155662.

[58] A. Dosovitskiy and T. Brox, "Generating images with perceptual similarity metrics based on deep networks," in Proc. Adv. Neural Inf. Process. Syst., 2016, pp. 658–666.

Hang Gao was born in 1995. She received the B.E. degree in electrical engineering from Southwest Jiaotong University, Chengdu, China, in 2016, and the M.S. degree, from the College of Electronic Science and Engineering, National University of Defense Technology, Changsha, China, in 2018. She is currently a Ph.D. student in information and communication engineering with the College of Electronic Science and Technology, NUDT.

Her research interests concentrate on radar signal processing and the analysis of wind field characteristics.

Chun Shen was born in 1985. He received the B.E. and M.E. degrees in information and communication engineering and the Ph.D. degree in information and communication engineering on the analysis of parameter retrieval and behavior prediction of aircraft wake vortex from the College of Electronic Science and Technology, National university of Defense Technology (NUDT), Changsha, China, in 2006, 2008, and 2021, respectively.

He is currently working as an Assistant Researcher with the College of Electronic Science and Engineering, NUDT. His research interests include aircraft wake vortex detection and wind filed hazard assessment.

Yi Zhou was born in 1979. He received the B.E. and M.E. degrees in aerospace science from the College of Aerospace Science and Engineering, National University of Defense Technology, Changsha, China, in 2002 and 2006, respectively.

His research interests include shipboard aircraft design and related technologies.

Xuesong Wang was born in 1972. He received the B.Sc. and Ph.D. degrees in information and communication engineering from the College of Electronic Science and Engineering, National University of Defense Technology (NUDT), Changsha, China, in 1994 and 1999, respectively.

He is currently a Professor with NUDT, where he is also the Dean of the College of Electronic Science and Technology. His research interests include radar information processing and target recognition.

Dr. Wang is a Fellow the Chinese Institute of Electronics. He was the recipient of one of the 100 excellent Ph.D. dissertations for his Ph.D. dissertation, China, in 2001 (two years after his graduation).

Pak-Wai Chan is an Assistant Director of the Hong Kong Observatory, Hong Kong, responsible for weather forecasting and warning services for the public. He received the B.Sc. and M.Phil. from the Physics Department of the University of Hong Kong. He has been working with the Hong Kong International Airport, Hong Kong, for over 20 years. He is a Visiting Professor with a number of universities in mainland China and an adjunct Associate Professor with the University of Hong Kong, Hong Kong. He has authored or coauthored more than 260 papers in SCI journals, with a significant portion of the papers focusing on the applications at the airport. His research interests include airport meteorological instrumentation, low level windshear and turbulence alerting, and high resolution numerical weather prediction.

Dr. Chan is a Fellow of the Royal Meteorological Society and a Chartered Meteorologist. He is a vice chair of the Expert Team of Upper Air Measurement at World Meteorological Organization and a chair of a working group of International Civil Aviation Organization in Asian region.
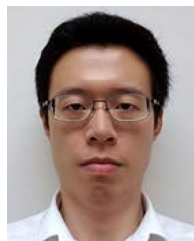
Kai-Kwong Hon received the B.A. degree in natural sciences and M.Sc. in experimental and theoretical physics from the University of Cambridge, U.K., in 2008. is currently an Acting Senior Scientific Officer with the Hong Kong Observatory, Hong Kong. Over the past decade, he has been actively involved in technical developments of the remote sensing and fine-resolution modelling of complex airflow around the Hong Kong International Airport, including long- and short-range LIDAR applications, aircraft wake turbulence measurements as well as numerical weather prediction down to the large eddy simulation (LES) regime. His research interests include data assimilation and predictability of high-impact weather events.

Dingfu Zhou was born in 1967. He received the B.S. degree in applied physics and the M.S degree in atomic and molecular physics and the Ph.D degree in optical engineering from the College of Electronics and Information Engineering, from Sichuan University, Chengdu, China, in 1989, 1994, and 2005, respectively.

Since 1994, he has been engaged in Laser and Lidar researches with the South-West Institute of Technical Physics (SWITP), Chengdu, China. He is currently working as a Full Researcher with SWITP. His research interests include laser instrument design, optical detection technology, wind Lidar, and related applications.

Jianbing Li (Senior Member, IEEE) was born in 1979. He received the B.E. and M.E. degrees in aerospace science and the Ph.D. degree in information and communication engineering, for his work on the analysis of wake vortices' scattering characteristics, from the College of Electronic Science and Engineering, National University of Defense Technology (NUDT), Changsha, China, in 2002, 2004, and 2010, respectively.

Dr Li is currently working as a Full Professor with the College of Electronic Science and Engineering, NUDT. His research interests include new concept radar design and distributed soft target detection.